Electron plasma expansion rate studies on the Electron Diffusion Gauge experimental device

Kyle A. Morrison, Stephen F. Paul, and Ronald C. Davidson
Princeton Plasma Physics Laboratory, Princeton University, Princeton, New Jersey 08543

The expansion of pure electron plasmas due to collisions with background neutral gas atoms in the Electron Diffusion Gauge experimental device is observed to be in good agreement with the predictions of a macroscopic fluid model with uniform electron temperature. Measurements of the expansion with a two-dimensional (2-D), phosphor-screen density diagnostic suggest that expansion rates measured with the 1-D diagnostic were observed concurrently with substantial changes in the plasma that are not due to electron-neutral collisions. Measurements of the on-axis, parallel plasma temperature evolution support this conclusion and further indicate that the plasmas are continuously losing energy during the expansion, presumably through inelastic collisions with trace background gases. © *2005 American Institute of Physics*. [DOI: 10.1063/1.1952828]

I. INTRODUCTION

Pure electron plasmas are trapped in the Electron Diffusion Gauge (EDG) experimental device,[1–4] a cylindrically symmetric, Malmberg–Penning trap[5–12] with inside diameter I.D.$=2\times R_w=5.08$ cm. Malmberg–Penning traps have a uniform magnetic field parallel to the common axis of several cylindrical electrodes, and particles with the same sign of charge can be confined by charging two nonadjacent electrodes to a sufficiently large voltage. Previously reported experimental results from the EDG experiment[2] indicate that the plasma expansion rates measured in the high-vacuum regime (where asymmetry-induced expansion is negligible) are in good agreement with the predicted expansion rates[13] derived using a warm fluid treatment of the plasma. The evolution of the inferred perpendicular temperature during this expansion, however, did not account for the clear decrease in electrostatic potential energy, prompting improvements to the EDG diagnostic systems.

In this paper, further measurements[4,14,15] of the plasma expansion and temperature evolution are reported. The diagnostics used for these measurements are described, and expansion rate data taken with the original density diagnostic are presented. New measurements made with a two-dimensional (2-D) phosphor-screen density diagnostic extend these density profile evolutions to much later times ($t \sim 20$ s), and an initial evolution of the plasma apparently unrelated to electron-neutral collisions is observed. Measurements of the on-axis plasma temperature evolution and estimates of the related change in the electrostatic potential energy as the plasma expands are also discussed.

II. ELECTRON DENSITY AND TEMPERATURE DIAGNOSTICS

To take density measurements in EDG, one of the charged cylindrical electrodes is quickly set to $V_c=0$ V and the entire electron plasma flows out of the trap axially (along the magnetic field) into a diagnostic. Axially integrated density profiles are obtained with a Faraday-cup density diagnostic[14,16] by accumulating measurements from a series of plasmas of the number of electrons passing through a small hole in a radially movable collimating plate. The particles moving along the magnetic field lines aligned with the small hole pass through to a Faraday cup, and the measurements from this Faraday cup at several radii give the radial profile. An example of the profiles obtained with this diagnostic is shown in Fig. 1. By forming several (well-reproduced) plasmas in succession, the evolution of these line-integrated, radial density profiles is obtained and used to follow the detailed expansion of the plasma.

Because many plasmas are needed to construct one measured density profile using the Faraday-cup diagnostic and the trap conditions tend to drift with time, it is difficult to make reliable profile measurements for plasmas held in the trap much longer than a second. The Faraday-cup density diagnostic has therefore been replaced with a biased, phosphor-coated glass screen observed by a CCD camera, a setup based on the diagnostics developed by other groups.[17,18] The phosphor coating is covered with an aluminum coating, both to reflect excess light from the plasma source (a 1.27-cm-diameter spiral filament) and to act as an additional electrode. The aluminum coating is biased to a voltage 3 kV$\leq V_s \leq$ 5 kV so the approaching electrons gain a sufficient amount of energy to penetrate the aluminum coating and excite the phosphor molecules underneath. The light emitted by the phosphor molecules passes through the glass screen, a glass vacuum window, a notch filter tuned to the peak emission wavelength of the phosphor (for P-43, 545 nm$\pm$2 nm, with a full width at half-maximum of 30 nm$\pm$6 nm), an f$=1.5$ camera lens, and a separate image intensifier on its way to the CCD camera.

A grounded, 10 wires/inch copper grid is attached to the last cylindrical trap electrode, which is about 2.5 cm from the biased screen. This grid makes the accelerating electric field more uniform, reducing the distortion of the plasma as it approaches the screen. The introduction of the grounded copper grid in the path of the exiting plasma allows some of the plasma electrons to experience large electric fields as
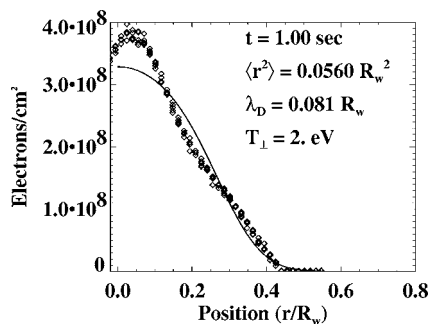
FIG. 1. This density profile is an example of data obtained with the Faraday-cup diagnostic, where each data point is obtained from a different plasma. The solid line represents a fitted, thermal quasi-equilibrium profile [see Eq. (1)].

they pass through, sometimes resulting in a grid pattern on the phosphor screen of either enhanced illumination or depressed illumination (depending on the combination of phosphor screen bias voltage V_s and magnetic field B). It is thought that the focused-electron patterns are caused by deflection of the electrons into the shadow of the grid by their attraction to the grid. The similar, defocused-electron patterns formed at other magnetic fields presumably arise because the electrons are deflected further, past the shadows of the grid wires. To improve the quality of the image data from the phosphor screen, images with enhanced-illumination grid patterns ("focused-electron" patterns) are preprocessed by masking out the characteristic grid-spaced peaks from their two-dimensional fast-Fourier transforms (FFTs). The FFTs for depressed-illumination grid patterns ("defocused-electron" patterns) are quite similar to those for enhanced-illumination grid patterns (the grid "lines" in the pattern are not extremely sharp, and comparable in width to the distance between them), so the same masking is applied to them and images with no apparent pattern, as well.

The density profile in Fig. 2 illustrates the improved resolution of the phosphor-screen diagnostic. The better agreement with the fitted density profile (the solid line) is primarily due to the different conditions used to form the plasma, and the discrepancies between the phosphor-screen diagnostic data and the fitted profile for $r/R_w < 0.2$ are simply due to noise in the images.

In Fig. 1, each diamond represents the number of electrons gathered from an individual plasma divided by the col-
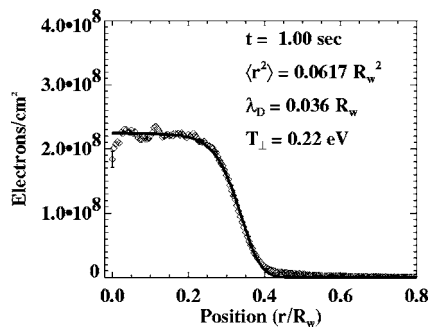
FIG. 2. This density profile is an example of the CCD-image-derived profiles, also overlaid with a fitted, thermal quasi-equilibrium profile.

limating hole area when the center of the collimating hole in the aluminum plate was at the corresponding radial position. It took approximately 6 min to record this profile. In Fig. 2, the diamonds represent the median intensity recorded by the CCD pixels in a ring of width $\delta r \approx 0.012$ cm (the width a pixel sees on the screen) that is centered on the centroid of the plasma's image. The intensity data recorded from the CCD image are scaled according to the total amount of charge drawn by the phosphor screen during the absorption of the plasma, which is measured with a charge-sensitive amplifier capacitively coupled to the phosphor-screen's charging circuit. The uncertainty in the profile is illustrated by the scatter in the data in Fig. 1, and by the error bars plotted on every tenth point in Fig. 2.

The perpendicular electron temperatures displayed in Figs. 1 and 2 are estimated by fitting an ideal, thermal quasi-equilibrium density profile to the measured, axially integrated profile. The thermal quasi-equilibrium profile[13] is

$$n(r,t) = \hat{n}(t)\exp\left\{ \frac{e\phi(r,t) - e\hat{\phi}(t)}{T} - \frac{r^2}{\langle r^2\rangle(t)}\left(1 + \frac{N_L e^2}{2T}\right) \right\},$$
(1)

where $\hat{n}(t)$ is the density at $r=0$ ("on axis") as a function of time, $\phi(r,t)$ is the electrostatic potential (obtained self-consistently from the solution of Poisson's equation, $\nabla^2\phi = 4\pi ne$), $\hat{\phi}(t)$ is the electrostatic potential at $r=0$. T is the electron temperature, N_L is the plasma line density $N_L = \int_0^{R_w} dr\, 2\pi r n(r)$, and $\langle r^2\rangle(t)$ is the mean-square radius $\langle r^2\rangle \times (t) = [\int_0^{R_w} dr\, 2\pi r r^2 n(r,t)]/N_L$. This thermal, quasi-equilibrium density profile describes expanding, infinite-length, azimuthally symmetric plasmas that enjoy global energy conservation, experience elastic electron-neutral collisions, and have a spatially uniform temperature (T independent of r). Poisson's equation can be recast in a form that shows the underlying profile shape $[\eta(\rho,t) \equiv 2\pi\langle r^2\rangle \times (t)n(r,t)/N_L$, where $\rho = r/\sqrt{\langle r^2\rangle}]$ is dependent on only one parameter, γ. This parameter is defined by $\gamma \equiv (\omega_r\omega_{ce} - \omega_r^2)/(\hat{\omega}_p^2/2) - 1$, where $\omega_{ce} = eB/m_e c$ is the electron cyclotron frequency, ω_r is the plasma rotation frequency, and $\hat{\omega}_p$ is the plasma frequency at $r=0$. In addition to varying γ, we also allow $\hat{n}(t)$ to vary in the fit for simplicity, though in principle it should be identifiable from the data.

On-axis parallel temperature measurements are also performed, using a technique described by Eggleston:[19] the charge on one of the confining electrodes is slowly decreased, and the number of electrons escaping the trap as a function of time is recorded. The results are fit using the approximate relationship

$$\frac{d\ln(Q_{esc})}{d(e\phi_c)} = \frac{-1.05}{T_\parallel},$$
(2)

where Q_{esc} is the total amount of charge that has escaped, $-e$ is the charge of an electron, ϕ_c is the confining voltage at $r=0$, and $T_\parallel$ is the parallel temperature in eV. In EDG, an improved charge-sensitive amplifier is capacitively coupled to the biased phosphor screen in order to measure the total charge that has escaped as a function of time. The voltage on
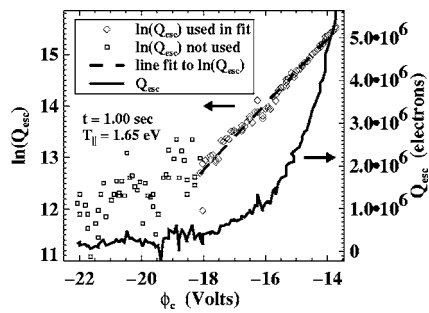
FIG. 3. Total charge escaped versus confining voltage as the plasma is released from the trap. The diamonds denote the data used in the fit, and the solid curve next to the right-pointing arrow is the raw data $[Q_{esc}(\phi_c(t))]$. These data were taken at a magnetic field of $B=600$ G, background gas pressure $P \sim 6 \times 10^{-9}$ Torr, filament heating voltage $V_h = 4.8$ V (the voltage difference between the center and the edge of the spiral filament), and filament bias voltage $V_b = -16.6$ V (the voltage at the center of the spiral filament). The plasmas measured each comprised $N \sim 5 \times 10^8$ electrons.

the confining electrode is decreased more slowly by inserting an RC circuit between it and the biasing amplifier. An illustrative plot of both $\ln(Q_{esc})$ versus ϕ_c and Q_{esc} versus ϕ_c is displayed in Fig. 3.

In Fig. 3, the solid line depicts the data produced by the improved charge-sensitive amplifier, and its scale is located on the right-hand side of the plot. The diamonds and squares show the natural logarithm of that data, with the scale located on the left side of the plot. The data represented by diamonds are the only data fit with the relationship in Eq. (2), and the dashed line obscured by the diamonds is the result of the fit. The voltage on the 5.08-cm-long cylindrical electrode is measured as the electrons leak out of the trap, and is fit with an RC-time-decay function to obtain the voltages used to plot the points in Fig. 3 and used when fitting Eq. (2) to the $\ln(Q_{esc})$ data.

III. MEASUREMENTS OF PLASMA EXPANSION

The plasma expansion rate referred to in this paper is the rate of change of the plasma mean-square radius ($d\langle r^2 \rangle / dt$). The mean-square radius for a long plasma column is determined with the equation

$$\langle r^2 \rangle = \frac{\int_0^{R_w} dr\, 2\pi r r^2 Q(r)}{\int_0^{R_w} dr\, 2\pi r Q(r)}, \tag{3}$$

where $Q(r)$ is the axially integrated density profile determined from a density diagnostic. For the Faraday-cup density diagnostic in EDG, $Q(r)$ corresponds to the axially integrated electron density averaged over the collimating hole area ($R_{hole} = 0.159$ cm) centered at location r. For the phosphor-screen diagnostic, $Q(r)$ corresponds to the median of the axially integrated electron density averaged over a CCD pixel area for pixels with centers between r and $r + \delta r$ ($\delta r \approx 0.012$ cm, the width on the screen of one camera pixel's view) from the centroid of the plasma's image.

The plasma expansion rate as a function of pressure was measured using the Faraday-cup density diagnostic for plas-
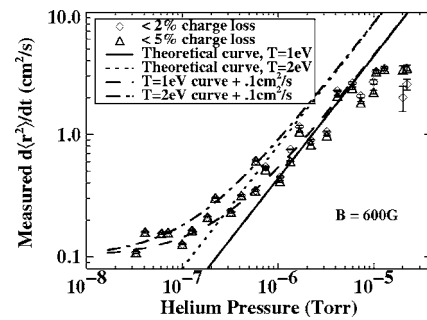
FIG. 4. Small-filament-plasma expansion rate plotted versus pressure for $B=600$ G. For these data, the plasmas comprised $4.9 \times 10^8 < N < 5.3 \times 10^8$ electrons (line density $N_L \approx 5.1 \times 10^8$ electrons/15 cm $= 3.4 \times 10^7$ electrons/cm), $V_h = 5.6-6.8$ V, and $V_b = -16.6--17.3$ V.

mas formed with a smaller filament ($R_f = 0.635$ cm) than was used for previous expansion rate measurements[2] (where $R_f = 1.27$ cm). These initially smaller plasmas were measured to determine whether the initially larger plasmas were interacting with the trap electrodes as they expanded, a situation which could explain their unexpected increase in inferred perpendicular temperature at $B=300$ G. The new plasma expansion rates at $B=600$ G are shown in Fig. 4, and those at $B=300$ G are shown in Fig. 5. Helium gas is fed into the chamber at different, controlled rates to vary the background gas pressure in these plots. The diamonds denote expansion rates computed using only the data taken at times before the plasma total charge had decreased by 2%, and the triangles refer to expansion rates computed using only the data taken at times before the plasma total charge had decreased by 5%. This distinction is important primarily at the higher pressures, where the measured total charge dropped quickly.

The data in Fig. 4 increase with pressure similarly to the $B=600$ G large-filament data observed previously, but are more consistent with the expansion rate curve predicted using a plasma temperature of $T=1$ eV than the curve using $T=2$ eV. The plasma expansion rate calculated[13] for azimuthally symmetric, uniform-temperature (T independent of r) plasmas affected by elastic collisions with background neutral gas is
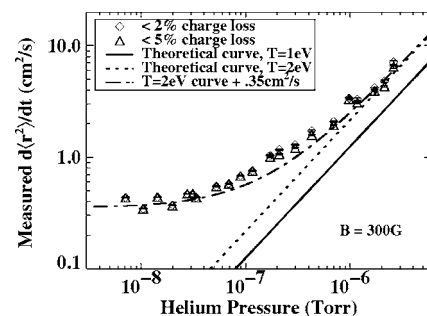
FIG. 5. Small-filament-plasma expansion rate plotted versus pressure for $B=300$ G. For these data, the plasmas comprised $4.75 \times 10^8 < N < 5.12 \times 10^8$ electrons (line density $N_L \approx 4.95 \times 10^8$ electrons/15 cm $= 3.3 \times 10^7$ electrons/cm), $V_h = 5.6-6.5$ V, and $V_b = -16.6--17.3$ V.
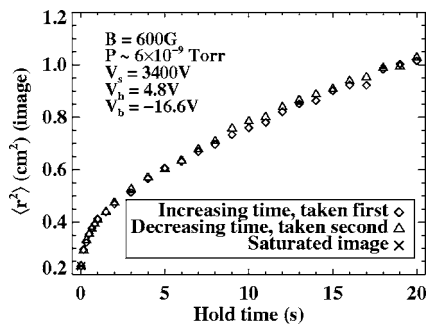
FIG. 6. Plasma mean-square radius as a function of time for the same experimental parameters as the data in Fig. 3. The agreement between the data taken while increasing the evolution times and that taken while decreasing the evolution times indicate the plasmas' reproducibility.

FIG. 7. Plot of the inferred perpendicular temperature for the same experimental parameters as the data in Fig. 3.

$$\frac{d}{dt}\langle r^2 \rangle = \frac{2 N_L e^2 \nu_{en}(T)}{m_e \omega_{ce}^2}\left(1 + \frac{2T}{N_L e^2}\right), \tag{4}$$

where $\nu_{en}(T) = n_n \sigma_{en} v_T$ is the electron-neutral collision frequency, T is the plasma temperature (in ergs), and N_L is the line density of the plasma column. The discrepancy at high pressures between the new expansion rate data and both the expansion rate predictions (the curves) and the previous measurements (not shown) is thought to be caused by quickly growing $m=1$ diocotron modes that could confound the Faraday-cup density diagnostic. The $m=1$ mode's growth rate in EDG is a strong, increasing function of the filament heating voltage,[14] and the heating voltage was increased to $V_h = 6.8$ V at these high pressures to maintain an approximately consistent number of plasma electrons. The departure of the data from the dotted and solid curves at the lowest pressures in Figs. 4 and 5 is expected, as previous measurements[1,2,20] of the expansion rate showed similar effects. It was hypothesized that these effects were caused by asymmetries that are not a function of pressure and dominate at sufficiently low pressures. The scatter in the data suggests that there are systematic errors in the measurements that are larger than the instrumental and calculation error displayed, presumably from uncontrolled variations in the trap conditions.

The plasma expansion rates at $B=300$ G displayed in Fig. 5 show more convincing agreement with the predicted dependence (using $T=2$ eV) and the data taken previously with the larger filament (not shown), probably because the faster plasma expansion is easier to measure. Direct parallel temperature measurements are not available for the Faraday-cup diagnostic data, and temperature inferences could not be made from the relatively peaked profiles because of computational issues. It is therefore not known how representative the temperatures used for the expansion rate predictions are of the true plasma temperatures. The fact that the 300 G expansion rate data taken with the smaller filament agree well with the data taken previously with the larger filament shows that there are not any interactions between the larger-filament plasmas and the trap wall that affect the expansion rate measurements.

The new, phosphor-screen density diagnostic can observe the entire, axially integrated density profile of a single plasma. It allows us to measure the density evolution well past $t=1$ s, greatly reduces the time it takes to identify the expansion rate, and allows us to observe the plasma expansion even in the presence of azimuthal plasma waves (including the $m=1$ diocotron mode). The plasma mean square radius evolution in Fig. 6 illustrates the expansion of the plasma at times later than $t=1$ s. It shows that the plasma's expansion rate is changing much less after the plasma has been confined for about 3 s than it is initially (at $P \sim 6 \times 10^{-9}$ Torr), suggesting that comparisons between expansion rates determined from this "late-time" data (where $t > 3$ s) should better illustrate the pressure dependence of the collisionally induced expansion than those derived from "early-time" data (where $t < 3$ s). The density profiles for the plasmas in Fig. 6 trapped longer than 3 s are fit somewhat better by the thermal quasi-equilibrium profiles than those for the plasmas trapped for less than 3 s, but the temperatures in Fig. 7 inferred from those fits hardly vary throughout the evolution. The corresponding, measured parallel temperatures at $r=0$ in Fig. 8, however, rise dramatically at the beginning of the evolution.
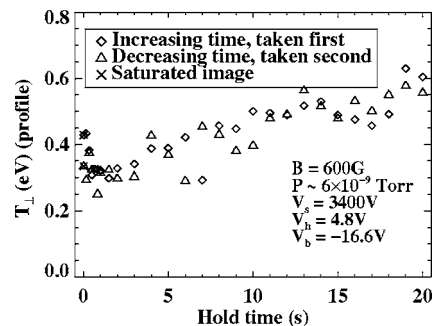
The most satisfying explanation available for this behavior is that the large changes in expansion rate for the early-time data are due to a dependence of the asymmetry-induced expansion on the plasma temperature, where the increase in plasma temperature caused by the asymmetry-induced expansion decreases the effectiveness with which asymmetries cause subsequent expansion. This would explain both the change in plasma temperature and the change in mean square radius. A similar dependence may be inferred from others'
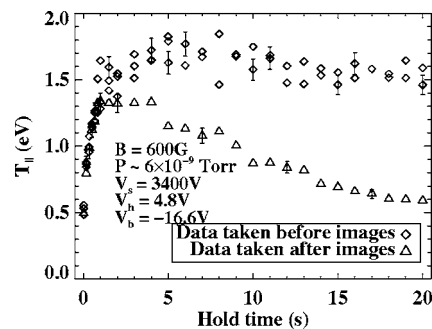
FIG. 8. Plot of the measured, on-axis parallel temperature evolution for the same experimental parameters as the data in Fig. 3.
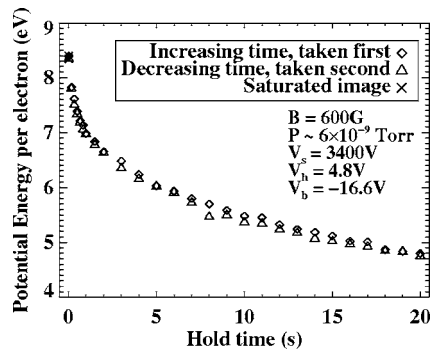
FIG. 9. Estimated electrostatic potential energy evolution determined from the axially integrated density profiles used to make the perpendicular temperature inferences in Fig. 7. The potential energy per electron is calculated by estimating the electric field from the axially integrated density profiles. The error bars estimated for these data are much smaller than the size of the plot symbols, and are omitted.

FIG. 10. Plot of the first 4 s of the measured, on-axis, parallel temperature evolutions using N_2 and helium as the background gas. For all three sets of data, the magnetic field was $B=600$ G and the filament bias voltage was $V_b=-16.6$ V. The filament heating voltage was $V_h=5$ V for the data taken in N_2, and $V_h=4.8$ V for the data taken in helium.

observations for magnetic or electrostatic asymmetries acting on electrostatically-trapped particles: (1) that the asymmetry-induced expansion rate (where the expansion rate is defined instead as $\nu_p \equiv (d\langle r^2 \rangle/dt)/\langle r^2 \rangle$) is proportional to the electrostatically-trapped-particle diocotron mode damping rate[21,22] and (2) observations and theory illustrating a decrease in electrostatically-trapped-particle diocotron mode damping rates with temperature.[23] However, Kabantsev *et al.*[21] suspect that asymmetry-induced expansion is most often caused by asymmetries acting on magnetically trapped particles instead of electrostatically trapped particles, and the relationship between the plasma expansion and the damping rate of magnetically trapped-particle modes has not been quantitatively observed. Alternatively, one may note that the radial particle flux due to resonances between plasma particles and asymmetries (where local particle trapping is not necessary) is also predicted[24–26] to decrease with increasing plasma temperature.

It is important to note that, since the measured parallel temperatures in Fig. 8 are only indicative of the temperature near $r=0$, the rapid increase in the first second of evolution does not necessarily indicate that the average plasma temperature is increasing that quickly. Indeed, the characteristic time for the plasmas to relax to a uniform temperature is estimated both by using the expression for classical collisions and Debye-length-scale interactions[8,27] (usually called $\mathbf{E} \times \mathbf{B}$ drift collisions) to be about $\tau_T \approx 0.5$ s. However, the average electrostatic potential energy per electron estimated from the observed density profiles (shown in Fig. 9) changes by $\Delta U \approx 1.5$ eV in the first second of the plasma evolution as well, suggesting that the measured parallel temperatures are more representative of the true plasma temperature than the inferred perpendicular temperatures.

The plasmas in Figs. 6–9 continue to expand after the initial evolution both because of trap asymmetries and electron-neutral collisions, but the measured parallel temperatures in Fig. 8 do not continue increasing. This suggests that the plasma is losing energy due to inelastic collisions with trace background gases.[16] This hypothesis is supported by the fact that the data taken approximately thirty minutes
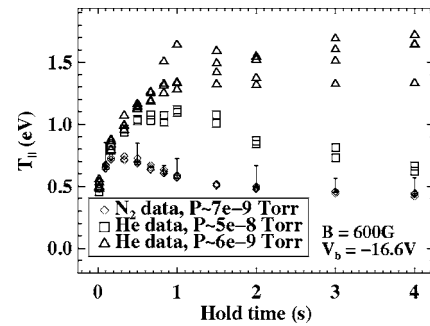
later in Fig. 8 (represented by the triangles) show a much more rapidly decreasing temperature than the data taken first (represented by the diamonds). The trace gases responsible are thought to be adsorbed to the trap surfaces and driven off gradually by heat from the filament, and it is observed that the partial pressure of the desorbed gas increases steadily after the filament is turned on.[14]

To appreciate the effect that trace background gas molecules can have on the plasma temperature,[28] N_2 gas was fed into the device instead of helium. Figure 10 shows the first 4 s of the parallel temperature evolution for plasmas with a primarily N_2 background gas environment (the diamonds) compared to temperature evolutions taken with helium gas environments [the triangles (both sets of data from Fig. 8) and the squares]. The error bars are omitted from the helium evolutions and only plotted for every fifth point in the N_2 evolution for clarity. It is clear that the N_2 background gas causes the plasmas' parallel temperature to drop much more dramatically than helium at a similar pressure and even helium at seven times the N_2 pressure. These data further support the hypothesis that trace background gases in EDG are responsible for abridging the anticipated increases in plasma temperature. (Note that the temperature data in Fig. 3 are only typical of the temperature data taken with helium as the background gas, and the temperature data taken with N_2 as the background gas had much lower background noise.)

The expansion rates measured with the Faraday-cup density diagnostic on EDG were determined from plasmas trapped less than 4 s (and usually less than one second), meaning that they were computed from plasmas experiencing the early evolution of the plasma that is presumably due to a temperature dependence of the asymmetry-induced expansion. It is still reasonable to make the comparison between the expansion rate measurements presented in Figs. 4 and 5 and the predicted rates, however, because the plasmas' expansion due to background gas is much faster than the asymmetry-induced plasma expansion at the higher pressures. Figure 11 shows a comparison of late-time expansion rates determined from the new small-filament profile data (excluding the initial evolution, where possible) to the expansion rates in Fig. 4. While the early-time expansion rates from Fig. 4 start to level off to a value of about 0.1 cm^2/s as
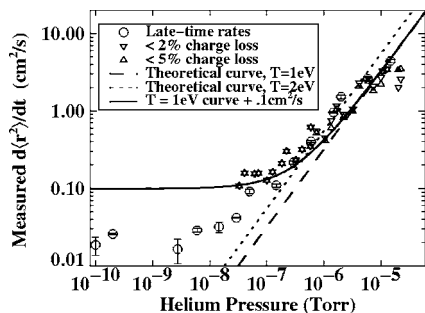
FIG. 11. Comparison of expansion rates determined with the Faraday-cup and phosphor-screen density diagnostics. The circles denote the new expansion rates computed by excluding the initial plasma relaxation where possible.

the background gas pressure decreases, the late-time expansion rates are clearly smaller. Estimating the expansion rates from the first second of the new phosphor-screen profile data at low pressures gives values that agree with that 0.1 cm^2/s value. Using late-time expansion rates allows us to make a better comparison between the predicted and measured expansion due to collisions with background neutral gas atoms.

IV. CONCLUSIONS

The theoretical curves in Fig. 11 agree with the data at higher pressures well, despite the fact that the collisionally induced expansion measured at higher pressures is accompanied by the mechanism causing the changing initial evolution shown at lower pressures. At higher pressures (above $P \sim 2 \times 10^{-7}$ Torr), the electron-neutral collision frequency is higher than the electron-electron collision frequency, so the temperature gradients that could exist in the plasma are also having a minimal effect on the expansion of the electron plasmas in EDG. It should also be noted that the cooling of the plasma through inelastic collisions with the trace background gases observed in Figs. 8 and 10 may also help explain the good agreement between the expansion rate data and the predicted rates using a constant temperature in Eq. (4).

[1] E. H. Chao, R. C. Davidson, S. F. Paul, and K. A. Morrison, Phys. Plasmas **7**, 831 (2000).
[2] K. A. Morrison, R. C. Davidson, S. F. Paul, E. A. Belli, and E. H. Chao, Phys. Plasmas **8**, 3506 (2001).
[3] E. H. Chao, R. C. Davidson, S. F. Paul, and K. A. Morrison, in *Proceedings of the 1999 Workshop on Nonneutral Plasmas: AIP Conference Proceedings 498*, edited by J. Bollinger, R. C. Davidson, and R. Spencer (AIP, Melville, NY, 1999), pp. 278–289.
[4] K. A. Morrison, R. C. Davidson, S. F. Paul, and T. G. Jenkins, in *Non-Neutral Plasma Physics IV: Workshop on Non-Neutral Plasmas: AIP Conference Proceedings, Volume 606*, edited by F. Anderegg, L. Schweikhard, and C. F. Driscoll (AIP, Melville, NY, 2002), pp. 416–421.
[5] J. S. deGrassie and J. H. Malmberg, Phys. Rev. Lett. **39**, 1077 (1977).
[6] T. M. O'Neil, Phys. Scr. **59**, 341 (1995).
[7] R. W. Gould, Phys. Plasmas **2**, 2151 (1995).
[8] C. F. Driscoll, F. Anderegg, D. H. E. Dubin, D. Z. Jin, J. M. Kriesel, E. M. Hollmann, and T. M. O'Neil, Phys. Plasmas **9**, 1905 (2002).
[9] F. Anderegg, N. Shiga, D. H. E. Dubin, C. F. Driscoll, and R. W. Gould, Phys. Plasmas **10**, 1556 (2003).
[10] J. J. Bollinger, J. M. Kriesel, T. B. Mitchell, L. B. King, M. J. Jensen, W. M. Itano, and D. H. E. Dubin, J. Phys. B **36**, 499 (2003).
[11] R. G. Greaves and C. M. Surko, Nucl. Instrum. Methods Phys. Res. B **192**, 90 (2002).
[12] J. Fajans, E. Gilson, and E. Y. Backhaus, Phys. Plasmas **7**, 3929 (2000).
[13] R. C. Davidson and D. A. Moore, Phys. Plasmas **3**, 218 (1996).
[14] K. A. Morrison, Ph.D. thesis, Princeton University (2004).
[15] K. Morrison, S. F. Paul, and R. C. Davidson, in *Non-Neutral Plasma Physics V: Workshop on Non-Neutral Plasmas: AIP Conference Proceedings, Volume 692*, edited by M. Schauer, T. Mitchell, and R. Nebel (AIP, Melville, NY, 2003), pp. 75–80.
[16] E. H. Chao, Ph.D. thesis, Princeton University (1999).
[17] A. J. Peurrung and J. Fajans, Rev. Sci. Instrum. **64**, 52 (1993).
[18] X.-P. Huang, K. S. Fine, and C. F. Driscoll, Phys. Rev. Lett. **74**, 4424 (1995).
[19] D. L. Eggleston, C. F. Driscoll, B. R. Beck, A. W. Hyatt, and J. H. Malmberg, Phys. Fluids B **4**, 3432 (1992).
[20] J. H. Malmberg and C. F. Driscoll, Phys. Rev. Lett. **44**, 654 (1980).
[21] A. A. Kabantsev, J. H. Yu, R. B. Lynch, and C. F. Driscoll, Phys. Plasmas **10**, 1628 (2003).
[22] A. A. Kabantsev and C. F. Driscoll, Phys. Rev. Lett. **89**, 245001 (2003).
[23] T. J. Hilsabeck and T. M. O'Neil, Phys. Plasmas **10**, 3492 (2003).
[24] D. L. Eggleston, Phys. Plasmas **4**, 1196 (1997).
[25] D. L. Eggleston and T. M. O'Neil, Phys. Plasmas **6**, 2699 (1999).
[26] D. L. Eggleston and B. Carrillo, Phys. Plasmas **10**, 1308 (2003).
[27] D. H. E. Dubin, Phys. Plasmas **5**, 1688 (1998).
[28] J. S. deGrassie and J. H. Malmberg, Phys. Fluids **23**, 63 (1980).